Improved corrosion and cavitation erosion resistance of laser-based powder bed fusion produced Ti-6Al-4V alloy by pulsed magnetic field treatment

Ma Mohin [a,*], Sufyan Akram [b], Anatolii Babutskyi [c,1], Andreas Chrysanthou [b], Edward P. Randviir [d], Aidan M. Doyle [d,*]

[a] School of Engineering, University of Bolton, Deane Road, Bolton BL3 5AB, UK
[b] School of Physics, Engineering and Computer Science, University of Hertfordshire, College Lane, Hatfield, Herts AL10 9AB, UK
[c] G.S. Pysarenko Institute for Problems of Strength, National Academy of Sciences of Ukraine, Kyiv 01014, Ukraine
[d] Department of Natural Sciences, Manchester Metropolitan University, Chester Street, Manchester M1 5GD, UK

ARTICLE INFO

ABSTRACT

The application of pulsed magnetic field (PMF) treatment demonstrated enhanced corrosion resistance in saline solution and prolonged resistance to cavitation erosion in deionised water for Ti-6Al-4V alloy manufactured by laser-based powder bed fusion (LPBF) and conventional wrought processing methods. The observed outcomes were attributed to the formation of a denser protective surface oxide layer and microstructural changes, resulting in a reduction of the α' phase by 0.13% and an increase in the presence of dislocations at the surface. Consequently, this led to an increase in the compressive residual stresses. Additionally, the application of this treatment resulted in the formation of highly refined and uniform precipitates, leading to a notable enhancement in microhardness by 5.73% and 5.85% for the conventionally manufactured (CM) and LPBF samples, respectively.

1. Introduction

Ti-6Al-4V alloy is used in a variety of applications including turbo-pump impellers [1] and dental implants [2] due to its high resistance to both corrosion and cavitation erosion. This resistance is due to a duplex microstructure that combines a hexagonal close-packed (HCP) α phase and a body-centred cubic (BCC) β phase [3], allowing the resistance parameters of the alloy to be optimised by modifying the volume ratio of the two phases. Such modifications currently rely on procedures that are time- and resource-consuming. Alternative procedures that reduce both time and resource costs will further enhance the attraction of Ti-6Al-4V in mission and endurance-critical applications. The use of 3D printing is an important development for the titanium processing sector and is expected to replace conventional subtractive material manufacturing; the inherent additive manufacturing advantages of 3D printing are characterised by the reduction of the number of production steps and by being a 'near-net-shape' manufacturing process [4]. The present study focuses on laser-based powder bed fusion (LPBF), which uses a sliced computer-aided design (CAD) model to produce high-quality Ti-6Al-4V components.

One of the important factors in the use of Ti-6Al-4V is the formation of a dense and protective surface oxide layer that provides corrosion resistance [5]; however, the oxide may degrade in chemically aggressive environments. In such environments, short-circuited micro-galvanic anode-cathode couples can be generated by factors such as surface roughness, grain size and composition, surface defects, and, in particular, non-uniform residual stresses as observed in other materials [6,7] and in commercially pure titanium [8]. In the case of layer-by-layer 3D printing, there exists a possibility for increased defect formation, which may restrict the use of this manufacturing technique. As a result, a number of research studies have assessed the corrosion resistance of 3D-printed Ti-6Al-4V [3,5,9–21]. These studies have shown that in the absence of post-treatment or careful consideration of build orientation (BO) for 3D-printed Ti-6Al-4V, there is reduction in corrosion resistance. For example, Chen et al. [13] reported oxidation induced by defects that were formed in direct metal laser sintering (DMLS) printed parts. In recent research investigations, the use of post heat treatment (HT) [5, 10–12,14,16] and BO [9,13,17,21] led to improved corrosion resistance in 3D-printed Ti-6Al-4V. In their work, Damborenea et al. [14] used direct metal laser sintering (DMLS) to produce Ti-6Al-4V surgical pins

* Corresponding authors.
E-mail addresses: m.mohin@bolton.ac.uk (M. Mohin), a.m.doyle@mmu.ac.uk (A.M. Doyle).
[1] Deceased.

and observed that manufacturing defects in the 3D-printed pins led to the formation of voluminous oxides leading to a reduction in corrosion resistance of the alloy when compared to wrought counterparts. The likely mechanism of the formation of these oxides was the presence of internal defects, which are an inherent feature of the manufacturing process. HT has recently been shown by various researchers, including Chandramohan et al., Xu et al. [15], Yang et al. [16] and Ettefagh et al. [5], to be beneficial in improving the corrosion resistance of 3D-printed Ti-6Al-4V. The improvement in corrosion resistance in these studies was reported to be caused by the transformation of the α' phase to the β phase in the alloy. By careful control of the BO, Chen et al. [13], Gong et al. [21] and Sui et al. [17] managed to improve the corrosion resistance of Ti-6Al-4V. Furthermore, Sui et al. [17] reported that selective laser melting (SLM) could lead to excellent corrosion resistance in both cross- and longitudinal-sections due to the presence of less acicular martensite (α') and to a greater amount of the β phase. In the study by Chen et al. [13], the effect of the 'anisotropic response' on the corrosion resistance of SLM-fabricated Ti-6Al-4V in terms of corrosion resistance in the XY, XZ, and YZ-planes was investigated. Overall, there was a higher corrosion resistance in comparison to a commercial rolled alloy. However, the YZ plane which was the cross-sectional plane perpendicular to the laser-moving direction produced inferior corrosion properties compared to the other two planes.

Studies by Dai et al. [3,9,10] compared the corrosion resistance of SLM-printed Ti-6Al-4V and traditionally processed Grade 5 alloy [3], both in the dimensions of the BO effect [9] and the HT effect [10]. Their analysis demonstrated that SLM-printed Ti-6Al-4V exhibited inferior corrosion resistance compared to the Grade 5 alloy [3,10]. The XZ-plane demonstrated lower corrosion resistance than the XY-plane [9], and subsequent HT reduced the corrosion resistance of SLM-produced Ti-6Al-4V [10]. The reduction in corrosion resistance was mainly attributed to the formation of metastable martensite [3,9,10] and to the increased grain size produced by HT as a result of the transformation of α'→α along with the associated formation of α + β phases [10].

Considerable efforts have been made to improve the surface properties of Ti-6Al-4V alloy using nitriding [22,23], laser alloying [24–26], plasma electrolytic oxidation coatings (PEO) [26,27] and peening methods [28] leading to an increase in the resistance against cavitation erosion. However, so far, there have been no studies dealing with PMF treatment to improve the resistance to cavitation erosion of 3D-printed titanium alloys. The present investigation has used a pulsed magnetic field (PMF) as a treatment method to improve resistance to corrosion and cavitation erosion. While a magnetic field has been shown to influence the corrosion behaviour of different alloys [29–31], the application of such a technique as a materials treatment process has not attracted much attention from the corrosion research community. An earlier study by Babutskyi et al. [8] showed improvement in the corrosion resistance of pure titanium; such improvement was attributed to the homogenisation of the dislocation substructure as a result of magnetic field treatment. Previous work has also shown that the process can lead to reduction in residual stresses [32–34] in other alloy systems and to improved tribological resistance [35,36]. A potential decrease in residual stresses is of interest as this can improve corrosion resistance. A literature search has shown that no previous studies have been conducted on the effect of PMF treatment on the corrosion behaviour of LPBF-produced alloys; in addition, there have been no previous studies to examine whether PMF treatment has any effect on the cavitation erosion resistance of titanium alloys.

The aim of the present study was to investigate the effect of PMF treatment on the corrosion and cavitation resistance of LPBF-produced Ti-6Al-4V relative to a conventionally manufactured (CM) alloy. Open circuit potential (OCP), potentiodynamic polarisation (PDP) and electrochemical impedance spectroscopy (EIS) tests were performed in phosphate-buffered saline (PBS) at room temperature in order to examine the corrosion behaviour. Cavitation erosion tests were also performed in deionised water at room temperature. Cavitation erosion

in impeller pumps occurs when the pressure at the discharge end becomes too high. Cavity development depends on the discharge pressure and the flow velocity incidence angle which affects the pressure distribution. The ASTM G32–10 standard [37] has been used in this study to produce cavitation damage on the surface of samples vibrated at high frequency in water. The vibration induces the formation and collapse of bubbles. The microstructural characterisation of Ti-6Al-4V alloys was conducted using scanning electron microscopy (SEM) and energy-dispersive X-ray spectroscopy (EDXS). Further characterisation using X-ray diffraction (XRD) and microhardness measurements for the treated and untreated alloys was also undertaken.

2. Experimental

2.1. Sample preparation

3D-printed and CM (i.e., wrought) Ti-6Al-4V cylindrical bars of 11 mm diameter were used for the investigation. The 3D-printed bar was LPBF-manufactured by Materialise, UK, in an EOSINT M 280 3D printer. The 3D-printed bar was built along the height direction, followed by HT. More details of the 3D printing production parameters can be found in [38]. The chemical composition of CM and LPBF produced bars were confirmed by EDX analysis to consist of 83.53±0.3 wt% Ti, 6.385 ±0.075 wt% Al and 3.47±0.04 wt% V, and 83.41±0.65 wt% Ti, 6.425 ±0.045 wt% Al and 3.33±0.15 wt% V, respectively. The bar sample was machined to a cylindrical test sample with diameter, d = 10±0.1 mm and thickness, h = 5±0.1 mm using an XYX Proturn SLX1630 CNC lathe. The top surface of the test samples was ground and polished up to a surface roughness of 0.6 μm. This was carried out to homogenise the surface roughness in accordance with the ANSI standard B74.18–1996 [39].

2.2. PMF treatment

PMF treatment was conducted at room temperature by placing each sample inside the bore of an inductor coil following sample preparation. A scheme of the PMF generator is shown in Fig. 2.1(A), while the orientation of the sample relative to the magnetic field is shown in Fig. 2.1(B). PMF generation can occur during the discharge of capacitors with a total capacity of up to 600 μF, charged up to 6 kV. An example of the registration of an electric current in the chain under the treatment used in the research is presented in Fig. 2.1(C). The treatment consisted of six pulses at two-minute intervals.

2.3. Corrosion testing

The corrosion tests were carried out in a PBS of pH 7.4 at room temperature using a standard electrochemical cell with three electrodes, which include a reference saturated calomel electrode (SCE), a counter electrode (platinum) and a 3.17 mm diameter (with geometrical surface area of 0.079 cm^2) disc as the working electrode. PBS (pH ~ 7.4) is commonly used in biological research, e.g., corrosion studies of dental implants. The PBS was made using 137 mM NaCl, 2.7 mM KCl, 10 mM Na$_2$HPO$_4$ and 1.8 mM KH$_2$PO$_4$. An Autolab PGSTAT101 potentiostat was employed to obtain the OCP curves over a duration of 1800 s. PDP curves were obtained using a sweeping range of −0.5 V/OCP to +1 V/OCP at a sweep rate of 1.0 mV/s. The cell was held at OCP for 30 minutes prior to potential sweeping to establish steady-state conditions at the working electrode surface. An Ivium CompactStat.h06125 was used to generate EIS curves using an alternating current (AC) amplitude of 10 mV over a frequency range of 10^{-2}-6×10^4 Hz at E=E$_{OCP}$. The EIS experimental data were fitted to an equivalent circuit model (Fig. 3.3(D)) that exhibited two time constants for electrode purposes to account for the effect of both the passive film formed on the metal surface as well as electrolyte penetration to the underlying metal surface where charge transfer reactions take place. To ensure
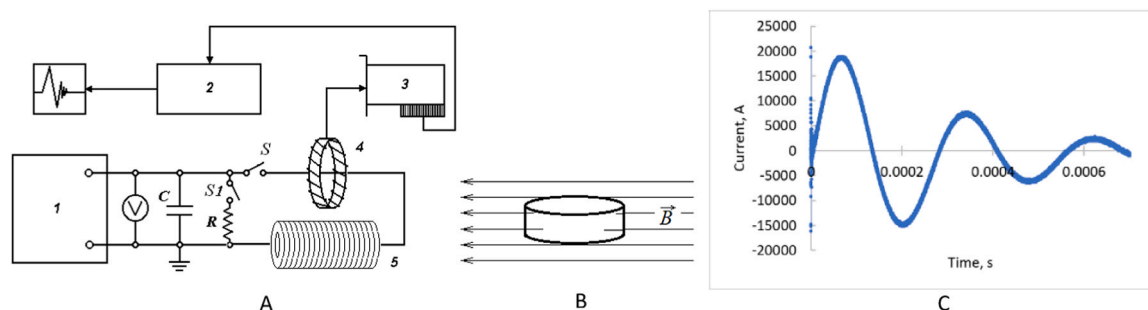
Fig. 2.1. Generator of PMF and data acquisition system (A): 1 – high voltage supplier, 2 – software, 3 – A-D converter, 4 – Rogowski coil, 5 – inductor with sample inside, S and S1 – switches, C – capacitors, R – ballast resistor; orientation of sample relative to the magnetic field (B); and example of recorded electrical current pulse in chain (C).

reproducibility of the experiment, the tests were run at least three times with fresh samples in each category of the Ti-6Al-4V, and only one of the results was shown in the Results section. The test surface was cleaned using acetone prior to the start of the test. The current density was calculated using the entire surface area of 0.079 cm^2.

2.4. Cavitation erosion testing

The cavitation erosion investigation for the magnetically treated and untreated conditions was conducted in compliance with the ASTM G32–10 standard [37] using the indirect method. The diameter of the sample was 10 mm. The test apparatus consisted of an ultrasonic horn (Vibra Sonic) with a titanium alloy tip, which worked at a maximum electrical peak power of 750 W, frequency of 20 ± 0.5 kHz and vibration amplitude of 50 μm. The test was performed in room temperature deionised water. Cavitation erosion studies are commonly conducted in deionised water. A heat exchanger tank was used to ensure that the test was conducted at a constant temperature of 25 ± 1 °C. The test specimen was kept 0.5 mm from the horn end. The mass loss was measured in eight hourly intervals using a precision balance (Denver Instrument). To increase the reliability of the results, the test was performed a minimum of three times for each sample condition, and the average values were used in the subsequent analysis.

2.5. Microstructural characterisation and residual stress analysis

The microstructure, imaging and EDX elemental analyses of the Ti-6Al-4V alloys were performed using a JEOL JSM-5700 LV scanning electron microscope (SEM). The samples were chemically etched using Kroll's reagent.

X-ray diffraction for phase identification was conducted using a PANalytical X'Pert diffractometer with a PixCEL 1-D detector using a Cu anode (kα$_1$ λ= 1.5406 Å) with the generator set at 45 mA and 40 kV. Data were collected over the range of 30–140° 2θ using a step size of 0.013° 2θ and a collection time of 118 s/step using automatic divergence and anti-scatter slits with an observed length of 5.0 mm. The results were processed using HighScore Plus Version 4.8.

RS measurements were obtained by using a Bruker D8 Advance X-ray diffractometer. The peaks evaluated for both the CM and LPBF-produced Ti-6Al-4V were 2Θ = 129° and 2Θ = 134°. The Sliding Gravity method was used to calculate the RS [40]. Leptos software, version 7.9, was used to improve the accuracy of the results, smoothing, Kα$_2$ correction, absorption correction and polarisation corrections. Vickers Microhardness tests were performed using a Struers DuraScan 20 microhardness tester. The microhardness values were presented by averaging 60 measurements across two radii for each sample at a load of 1 N.

3. Results

3.1. Evidence of improved corrosion resistance using an Open circuit potential (OCP)

Fig. 3.1 depicts the measured OCPs as a function of time for the Ti-6Al-4V alloys immersed in a PBS of pH 7.4 at room temperature.

The results in Fig. 3.1 demonstrate an initial shift in the surface potential, from negative potential tending towards positive potential, for all samples following immersion in the PBS solution. Equilibrium potential values were reached after approximately 300 seconds in all cases. This provides evidence that all the samples exhibited the same cathodic process without fluctuations. This shift in potential at the metal-electrolyte surface with time also indicates evidence of the formation of a passive film, i.e., a protective TiO$_2$ layer (1×10^{-9} m to 4×10^{-9} m) on the metal surface [11,15,41,42]. After 1800 s, the open circuit potential (OCP) for the CM alloy, the PMF-treated CM alloy, the LPBF-produced alloy and the PMF-treated LPBF-produced alloy was -0.32 ± 0.01 V, -0.19 ± 0.02 V, -0.18 ± 0.01 V and -0.14 ± 0.01 V, respectively, *versus* SCE. In both the conventional and LPBF cases, the PMF-treated alloy showed less negative OCP values compared with the untreated alloy, reflecting the formation of a more stable passive film at the surface, as suggested in [43]. Additionally, the LPBF-produced alloy showed a significantly less negative OCP value compared to the CM alloy suggesting a relatively more stable passive film formation for the LPBF-produced alloy.
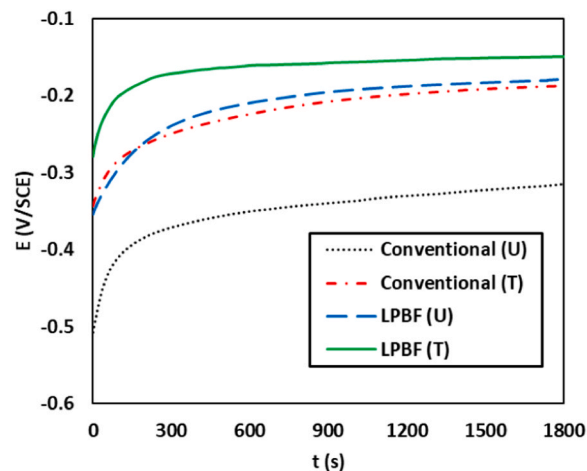

Fig. 3.1. OCP as a function of time for Ti-6Al-4V alloys immersed in PBS of pH 7.4 at room temperature. Here, U and T stand for Untreated and Treated, respectively.

3.2. Potentiodynamic polarisation (PDP)

Fig. 3.2 displays PDP curves (Fig. 3.2(A)) and the corresponding Tafel regions (Fig. 3.2(B)) for Ti-6Al-4V alloys immersed in PBS of pH 7.4 at room temperature. The corrosion parameters obtained from the PDP curves and Tafel plots are summarised in Table 3.1.

From the results, it is evident that the curves depicted in Fig. 3.2(A) show that all metal samples displayed active-passive behaviour where the active region translated into the passive region. The passive region consisted of nearly a constant current density, the average value of which is defined as the passivation current density, i_{pp} [5]. It is well known that a low value of i_{pp} indicates a low dissolution rate of the surface film [4]. The passivation potential, E_{pp}, on the other hand, is the starting point of the passivation region. Materials with more noble E_{pp} (i. e., closer to zero) are thermodynamically more stable. In this study, the LPBF-produced alloy showed a lower i_{pp} and a higher E_{pp} compared to the CM alloy (Table 3.1). There was a reduction of the i_{pp}, from 2968.95 $\mu A/cm^2$ to 316.16 $\mu A/cm^2$ and an increase in the E_{pp}, from 0.08 V to 0.17 V when comparing the two fabrication techniques. Furthermore, PMF treatment for both the LPBF-produced and CM alloys showed further decreases in i_{pp} and increases in E_{pp}. In the case of the CM alloys, the i_{pp} dropped from 2968.95 $\mu A/cm^2$ to 1482.46 $\mu A/cm^2$, while the E_{pp} increased from 0.08 V to 0.16 V, both changes being the direct result of PMF treatment. In the case of the LPBF alloys, the i_{pp} decreased from 316.16 $\mu A/cm^2$ to 122.78 $\mu A/cm^2$ and the E_{pp} increased from 0.17 V to 0.24 V again as a result of PMF treatment. These observations suggest that PMF treatment passivates the metal surface and thus increases its corrosion resistance. The corrosion current, i_{corr}, and potential, E_{corr}, for the Ti-6Al-4V alloy obtained by Tafel extrapolation [44] provided further evidence of the beneficial nature of the PMF treatment. In the case of the CM alloys, PMF treatment led to a reduction in the i_{corr} value from 67.24 $\mu A/cm^2$ to 19.55 $\mu A/cm^2$ and a reduction in the E_{corr} value from −0.35 V to −0.30 V. In the case of the LPBF-produced alloys, PMF treatment led to a reduction in the value of i_{corr} from 14.24 $\mu A/cm^2$ to 1.85 $\mu A/cm^2$ and a reduction in E_{corr} from −0.25 V to −0.21 V. In both cases, the PMF treatment led to a reduction in i_{corr}, leading to a reduction in the corrosion rate as a result of the PMF treatment. There was also an increase in the E_{pp} value making the alloy less prone to corrosion. Additionally, the LPBF-produced samples showed comparatively low i_{corr} and high E_{corr} values compared to the CM alloys. These experiments suggest that PMF treatment may be a promising technique for surface preparation of alloys, irrespective of the fabrication method of the alloy.

Table 3.1

Corrosion parameters obtained from PDP curves of the two Ti-6Al-4V alloys immersed in PBS of pH 7.4 at room temperature.

Sample	E_{corr} (V)	i_{corr} ($\mu A/cm^2$)	E_{pp} (V)	i_{pp} ($\mu A/cm^2$)
Conventional Ti-6Al-4V	-0.35 ± 0.02	67.24 ± 1.25	0.08 ± 0.003	2968.95 ± 794
PMF Conventional Ti-6Al-4V	-0.30 ± 0.01	19.55 ± 1.17	0.16 ± 0.01	1482.46 ± 331
LPBF Ti-6Al-4V	-0.25 ± 0.01	14.24 ± 0.16	0.17 ± 0.01	316.16 ± 40
PMF LPBF Ti-6Al-4V	-0.21 ± 0.01	1.85 ± 0.20	0.24 ± 0.03	122.78 ± 36

3.3. Electrochemical impedance spectroscopy (EIS)

Fig. 3.3 depicts the EIS measurements in the form of Nyquist (A) and Bode (B, C) plots alongside the equivalent circuit model (D) used to fit the experimental data. Table 3.2 shows the corresponding fitting parameters for the Ti-6Al-4V samples in PBS of pH 7.4 at room temperature. The parameters obtained by the proposed electrical circuit model $(R_s(Q_p(R_bQ_b)))$ are reliably used for comparison of the behaviour of the four samples because these parameters (R_s, R_p, Q_p, R_b and Q_b) can be compared appropriately. Good curve fitting was achieved for the EIS test (Fig. 3.3) and this was further confirmed by the chi-squared ($\chi 2$) value of about 10^{-4} [45] that is presented in Table 3.2. A similar circuit model was also used previously in corrosion studies of Ti-6Al-4V by other researchers [3,5,18].

The Bode plots in Fig. 3.3 (C) for the untreated conventional and LPBF samples and for the PMF-treated conventional samples each show two clearly defined humps as expected, indicating the presence of two time constants. Such a response suggests the presence of a porous outer layer (at a lower frequency) and a dense and compact inner layer (at a higher frequency). However, in the case of the PMF-treated LBPF alloy, the behaviour is not as clearly defined and the plot is dominated by the main hump. At first glance, it may appear that there is a removal of one of the time constants and that the electrode process has changed and therefore, the equivalent circuit model is non-equivalent. However, careful consideration of the Bode plot for this alloy may suggest the presence of an initial hump at the very beginning of the test at low frequency; this hump is not clearly pronounced, and it is followed by a second hump that dominates the behaviour and is suggestive of the presence of a dense protective oxide layer. From these results, it is apparent that there has been a change in the behaviour of the LBPF sample as a result of the PMF treatment. In fact, the results in Table 3.2 show that the cavitation resistance for the PMF-treated LBPF alloy is so
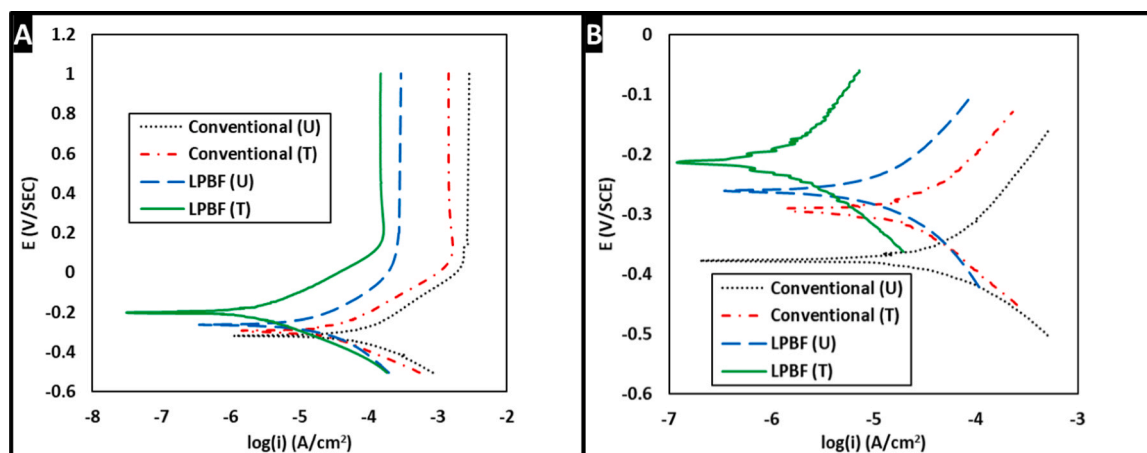

Fig. 3.2. (A) PDP curves for Ti-6Al-4V alloys in PBS of pH 7.4 at room temperature and (B) Tafel regions of the polarisation curves. Here, U and T stand for Untreated and Treated, respectively.
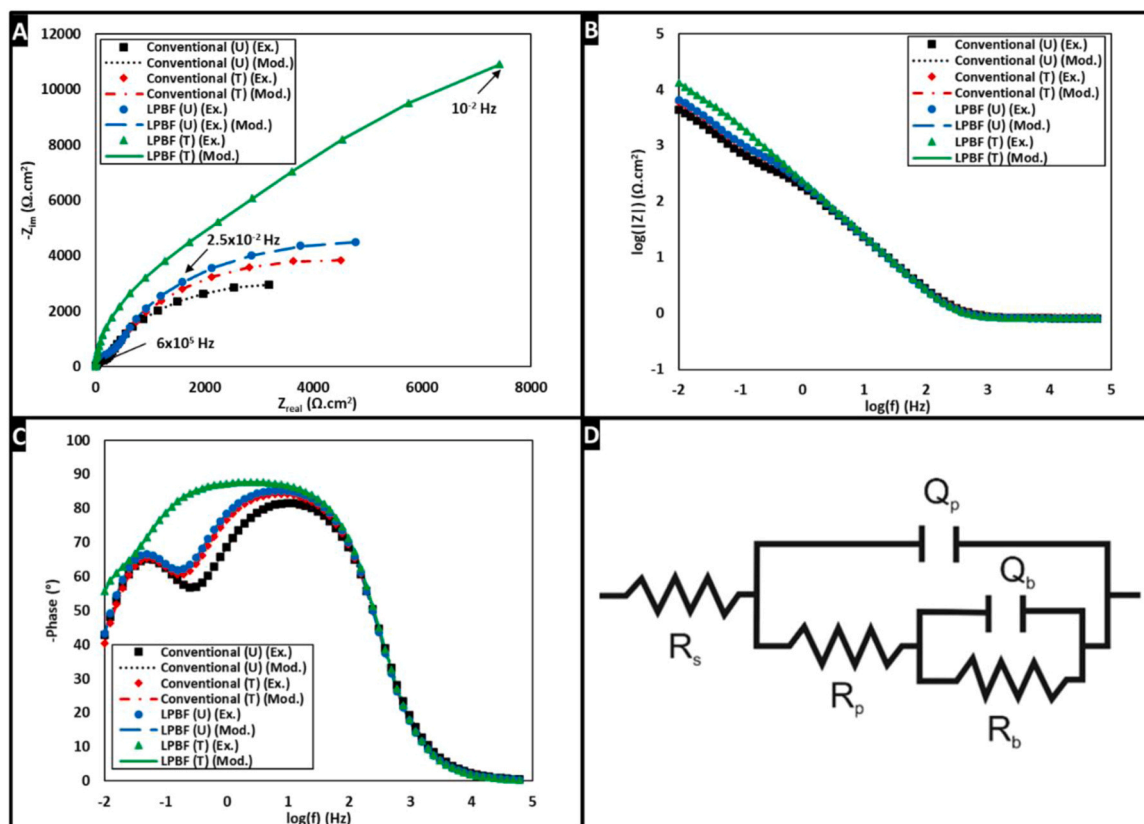
Fig. 3.3. (A) Nyquist plot, (B) and (C) Bode plots and (D) the corresponding electrical equivalent circuit for EIS test for Ti-6Al-4V alloys in PBS of pH 7.4 at room temperature. Here, U and T stand for Untreated and Treated, respectively.

Table 3.2
The curve filling parameters of EIS measurements obtained by an equivalent circuit for Ti-6Al-4V alloys in PBS of pH 7.4 at room temperature.

Sample	R_s ($\Omega.cm^2$)	$Q_p/10^{-4}$ ($F.cm^{-2}.s^n$)	N_p	R_p ($k\Omega.cm^2$)	$Q_b/10^{-3}$ ($F.cm^{-2}.s^n$)	N_b	R_b ($k\Omega.cm^2$)	$\chi2/10^{-4}$
CM Ti-6Al-4V	0.82 ±0.01	8.48±0.011	0.95±001	0.61 ±0.001	1.75±0.05	0.97 ±0.002	5.89±0.027	5.12±0.123
PMF-treated CM Ti-6Al-4V	0.85±0.02	7.79±0.22	0.97 ±0.0009	1.12±0.02	1.29±0.03	0.97 ±0.009	6.93±0.026	5.28 ±0.0.104
LPBF-produced Ti-6Al-4V	0.83±0.02	7.47±0.02	0.98±.0009	1.29±0.01	1.24±0.002	0.98 ±0.009	8.19±0.145	5.73±0.174
PMF-treated LPBF-produced Ti-6Al-4V	0.83±0.01	7.03±0.10	0.98±0.002	12.85 ±0.10	1.19±0.001	0.98 ±0.008	16.10 ±0.159	5.35±0.048

high to the point that there may not be much cavitation at all. The same equivalent circuit model has been maintained to allow comparison between the same parameters, but realistically, the increase in resistance to cavitation of the PMF-treated LPBF sample shows the material behaving more like a smooth non-porous electrode, so a model containing mixed kinetic and diffusion control (i.e., Randles cell) would perhaps be more appropriate for this sample and would explain the straight line tending to 45° in the Nyquist plot for PMF-treated LBPF alloy.

The calculated EIS parameters are listed in Table 3.2 and include the resistance of the electrolyte, R_s (PBS of pH 7.4), the non-Faradaic resistance and capacitance of the outer layer film of the studied material, R_p and Q_p, and the Faradaic resistance and capacitance to the charge transfer of the redox reaction associated with metal leaching (i.e., cavitation), R_b and Q_b [4]. It is well known that corrosion resistance can be estimated using the arc radius Nyquist plot, where a greater radius indicates improved corrosion resistance [5,46]. Fig. 3.3(A) shows unequivocally that PMF treatment enhances the corrosion resistance of the material as evidenced by the increase in the arc radius after PMF

treatment. The PMF-treated CM alloys exhibited an R_b value of 6.93 kΩ.cm^2, which was approximately 15% higher than the value for the untreated CM alloys (5.89 kΩ.cm^2). Similarly, the PMF-treated LPBF-produced sample exhibited the largest R_b value (16.10 kΩ.cm^2), which is almost twice that for the LPBF-produced alloys (8.19 kΩ.cm^2). Comparing the results of samples from the different manufacturing approaches, Fig. 3.3(A) shows clearly that LPBF fabrication led to an increase in the corrosion resistance of the material as evidenced by the increase in the arc radius when comparing the CM alloys (5.89 kΩ.cm^2) to the LPBF-produced alloy (8.19 kΩ.cm^2). Comparatively, these R_b values may appear to be low, but they are not uncommon in the literature and are attributed to defects in the β phase microstructure generating more active sites for the electrochemical reactions to take place [47].

Fig. 3.3(B) and (C) depict Bode plots for the samples that were tested. In all cases, the total impedance of the system became frequency-independent above 1000 Hz (Fig. 3.3(B)). This observation is supported by the phase angle plots presented in Fig. 3.3(C) which exhibit the phase angle reaching 0° at 10,000 Hz. Within this high-frequency

region, the impedance profile is shown to be dominated by the solution resistance, R_s [4]. In addition, the values for R_s were in all cases demonstrated to be within 0.03 $\Omega.cm^2$ of each other, indicating that the PMF treatment and alloy fabrication method did not affect this parameter. Fig. 3.3(B) shows that in all cases, as the frequency decreases, the total impedance of the system increases. Within the range of 10,000 Hz and about 10 Hz, the phase angle between the applied AC potential and the measured current shifts almost linearly from 0 to $-90°$, demonstrating that the system tends more towards 'capacitative' behaviour in this mid-frequency range [4,45]. This provides evidence of the formation of a protective film-like passive layer for all the samples in the solution. The near-straight line with a slope of -1 in low and middle frequencies (0.01 Hz to 100 Hz), as observed in Fig. 3.3(B) also confirms the capacitive behaviour of the passive film [45]. The higher phase angle which is considered to be an indication of higher corrosion resistance [5] can be linked to stable oxide film formation and to the difficulty in charge transfer [45]. As such, the order of the highest phase angle and therefore highest corrosion resistance of the samples used in this study was PMF+LPBF > LPBF > PMF+Conventional > Conventional. The phase angle (Fig. 3.3(C)) declined at frequencies below 1 Hz in the case of the CM alloys, PMF-treated CM and LPBF-produced alloys and below about 0.1 Hz in the case of the PMF-treated LPBF-produced alloy. In the latter case, there is a noticeable difference in the phase angle shift, whereby the 'peak' phase angle shift of $-55°$ at -0.5 log Hz has disappeared; instead the phase angle over the range of frequency between 0.1 Hz and 100 Hz seems to remain almost level and close to $-90°$. This provides evidence of the complete removal of one electrode process (at low frequency). It is therefore proposed that the PMF/LPBF alloy formed a more stable and potentially less porous oxide layer as a result of the combined approaches which have stabilised the surface sufficiently to minimise ion passage through the film. The absence of the second electrode process supports the claim that the surface oxide is more stable and is not prone to further degradation after the oxide layer is formed. Additionally, the modulus of impedance for the PMF-treated LPBF-produced alloy remained comparatively higher at low frequencies (<0). The EIS data demonstrate that the PMF-treated LPBF-produced Ti-6Al-4V alloy showed better corrosion resistance amongst all the materials used in this study and that coupling of the LPBF and PMF approaches may actually prevent ion migration through the oxide layer.

From Table 3.2, it is evident that the value of R_s was low and constant ($\sim$0.83 $\Omega.cm^2$), which indicates that the test condition remained unchanged throughout the study. According to Xie et al. [45], high resistance of R_p and R_b and low capacitance of Q_p and Q_b are indicators of improved corrosion resistance. Following this argument, consideration of the results in Table 3.2 suggest that the corrosion resistance of the materials used in this study followed an order of PMF+LPBF > LPBF > PMF+CM > CM. The derivation parameters (such as n_p and n_b) related to the phase shift [21] were found to be close to 1, a value which represents a near-capacitive behaviour of the passive oxide layer and is consistent with observations from a number of previous studies [4,21, 45].

3.4. Cavitation erosion behaviour

Fig. 3.4(A) shows the cumulative mass loss as a function of cavitation exposure time of up to 8 hours for Ti-6Al-4V alloy in deionised water. The standard deviation in the results is presented by error bars. Fig. 3.4 (B) represents the cumulative erosion rate vs exposure time plot obtained by differentiating the cumulative erosion-time curve as suggested by the ASTM G32–10 standard [37]. The erosion-time curves (Fig. 3.4 (A)) demonstrated the same pattern where the level of mass loss during the initial stages was low and gradually increased with time. The erosion rate-time curves (Fig. 3.4(B)) showed an acceleration stage, a maximum rate point and a deceleration stage; however, no incubation period was detected. A likely reason for not detecting an incubation period could be due to the use of a minimum time interval of one hour. The maximum erosion rate, the time to maximum erosion rate and mass loss after eight hours are shown in Table 3.3.

From Fig. 3.4(B) and Table 3.3, it is evident that the 3D-printed samples showed lower maximum erosion rates when compared with the CM alloy. Even though the maximum erosion rate for PMF-treated LPBF-produced Ti-6Al-4V was slightly higher than that of the LPBF-produced Ti-6Al-4V, the area under the dm/dt vs t graph for the treated sample is lower, which suggests an overall lower cavitation erosion for the treated alloys. In addition, the rate of mass loss for the PMF-treated LPBF-produced alloy was only temporarily higher after 6 hours of testing compared to the untreated samples. At all other test periods, the untreated LPBF Ti-6Al-4V exhibited a lower rate of mass loss. The mass loss for the CM Ti-6Al-4V alloy dropped by 17.99% following PMF treatment, and for the LPBF alloy, it decreased by 15.04%. The erosion rates for both PMF-treated samples were lower during the acceleration stage in comparison with the untreated ones.

Table 3.3
The maximum erosion rate, the time to maximum erosion rate and mass loss after 8 h.

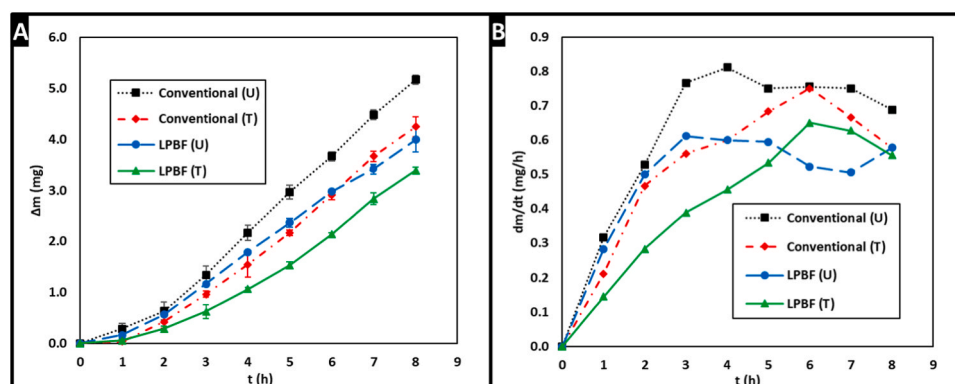| Sample	Maximum erosion rate (mg/h)	Maximum erosion rate time (h)	Mass loss after 8 h (mg)
CM Ti-6Al-4V	0.81	4	5.17 ± 0.09
PMF-treated CM Ti-6Al-4V	0.75	6	4.24 ± 0.20
LPBF-produced Ti-6Al-4V	0.61	3	3.99 ± 0.23
PMF-treated LPBF-produced Ti-6Al-4V	0.65	6	3.39 ± 0.07

Fig. 3.4. Cumulative mass loss (A) and corresponding cumulative mass loss rate (B) of Ti-6Al-4V alloys in deionised water during 8 h cavitation erosion testing.
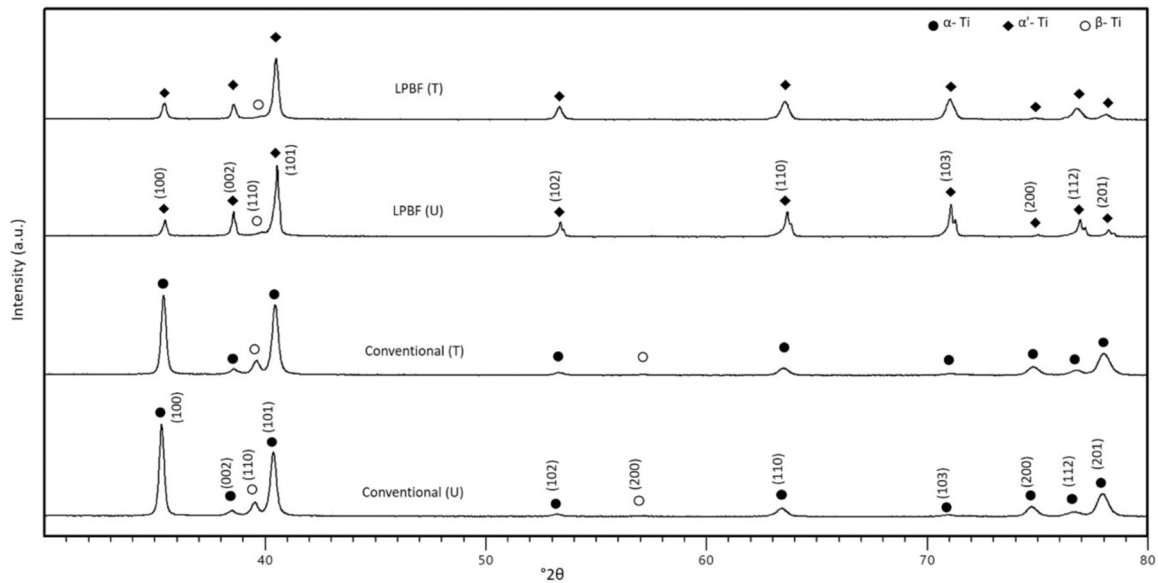
Fig. 3.6. XRD results of Ti-6Al-4V alloys.

LPBF samples is likely to promote formation of the α' phase. While the presence of minor levels of α cannot be fully discounted particularly during the slower cooling of the inner layers of the LPBF samples [52, 53], the low (100):(002) peak intensity ratio is suggestive of the dominance of the α' phase. It must also be noted that as expected the high rate of cooling associated with the LPBF samples has led to a decrease in the amount of the β phase [53].

For the CM alloy, the lattice parameters of the α phase are $a = 2.913$ Å and $c = 4.680$ Å with a c/a ratio of 1.607 and for the β phase $a = 3.223$ Å. Post-PMF treatment, the lattice parameters in the CM Ti-6Al-4V sample changed to $a = 2.933$ Å and $c = 4.680$ Å for the α phase with a c/a ratio of 1.596, and for the β phase $a = 3.223$ Å. So, post-PMF treatment, the ratio of c/a for the α phase decreased by 0.68%. This is an observation that is usually indicative of lattice distortion and occurs during processes such as annealing [54]. Based on Rietveld fitting the approximate proportion of the β phase is almost unchanged at between 8% and 10%.

In the case of the LPBF-produced Ti-6Al-4V, the lattice parameters of the α' phase are $a = 2.923$ Å and $c = 4.669$ Å with a c/a ratio of 1.597. The post-PMF treatment LPBF-printed Ti sample remains exclusively in the form of the α' (hcp') phase with lattice parameters $a = 2.931$ Å and $c = 4.674$ Å with a c/a ratio of 1.595. So, post-PMF treatment, the ratio of c/a for the α' phase was reduced by 0.13%. Following PMF treatment, there is a noticeable decrease in the intensity of the (002) peak. For example, the peak intensity ratio of (100):(002) has increased from 0.68 to 1.14, indicating a loss of the α' character, which has been demonstrated to be beneficial by previous studies [3, 5, 9–12] as α' is considered to be the metastable high energy phase prone to corrosion damage. The observed increase in the value of both the a and c lattice parameters of the α' phase following PMF treatment is also depicted by a very small shift in the XRD peaks of this phase to slightly lower diffraction angles. This is probably due to loss of vanadium from the α' phase as it transforms to α and β since this element is a β stabiliser. The atomic radius of vanadium (1.32 Å) is lower than that of titanium (1.47 Å) and aluminium (1.43 Å) and therefore loss of vanadium will lead to an increase in the lattice parameter of the α' phase [53].

There is a noticeable broadening of the peak profiles in the post-PMF sample, indicating an increase in dislocation density confirming the probable formation of microplasticity. Dislocation multiplication as induced by PMF treatment for pure Ti was found to be beneficial to corrosion resistance in a previous study by Babutskyi et al. [8] as it led to micro-electrical homogenisation of the metal surface. Additionally, the

microplastically induced work-hardening may have a positive impact on cavitation erosion resistance [55].

From the RS results (Table 3.4), it can be observed that the CM alloy contained tensile RS at the surface; such RS is detrimental to corrosion resistance [56,57] and cavitation erosion resistance [57], while the LPBF-produced Ti-6Al-4V contained compressive RS at the surface which improves the corrosion resistance by promoting passive film formation [7,56]. The enhanced atomic density [56] or reduced interatomic spacing [7] as a result of increased compressive RS or reduced tensile RS can promote passive film formation. The presence of more compressive RS [58] and lower tensile RS [59] is beneficial to cavitation erosion resistance by hindering crack initiation and propagation. In this study, the PMF treatment was able to reduce the tensile RS by 19 MPa in the CM alloy and increase the compressive RS by the same amount in the LPBF-produced alloy. This mitigation of tensile RS and the formation of additional compressive RS suggest that PMF treatment can improve the corrosion and cavitation erosion resistance of Ti-6Al-4V alloys. It must be noted that PMF treatment has previously been used to reduce tensile RS of multiple alloys [32–34].

3.7. SEM analysis

Fig. 3.7 shows the SEM images of Ti-6Al-4V surfaces after etching with Kroll's reagent.

The CM Ti-6Al-4V alloy consists of the α and β phases (dark and light area) (Fig. 3.7(A)). On the other hand, LPBF-produced Ti-6Al-4V contains needle-shaped α' along with β (dark and light area), which is consistent with other studies [5,16,17] (Fig. 3.7(C). Following the PMF treatment, both of the alloys, i.e., CM and LPBF-produced, show the appearance of new fine light-coloured precipitates which are distributed throughout the samples (Fig. 3.7(B, D)). The observed loss of the α' character, as shown by the XRD results, suggests that these microstructural changes are taking place as a result of precipitation of α and β. Similar changes were reported by other researchers [17,60,61] as a result of HT.

3.8. Microhardness measurements

Fig. 3.8 shows a comparison of microhardness measurements for the treated and untreated CM and LPBF-produced samples.

From the data, it is apparent that the microhardness of LPBF-produced Ti-6Al-4V was 8.74% higher than that of the CM Ti-6Al-4V.
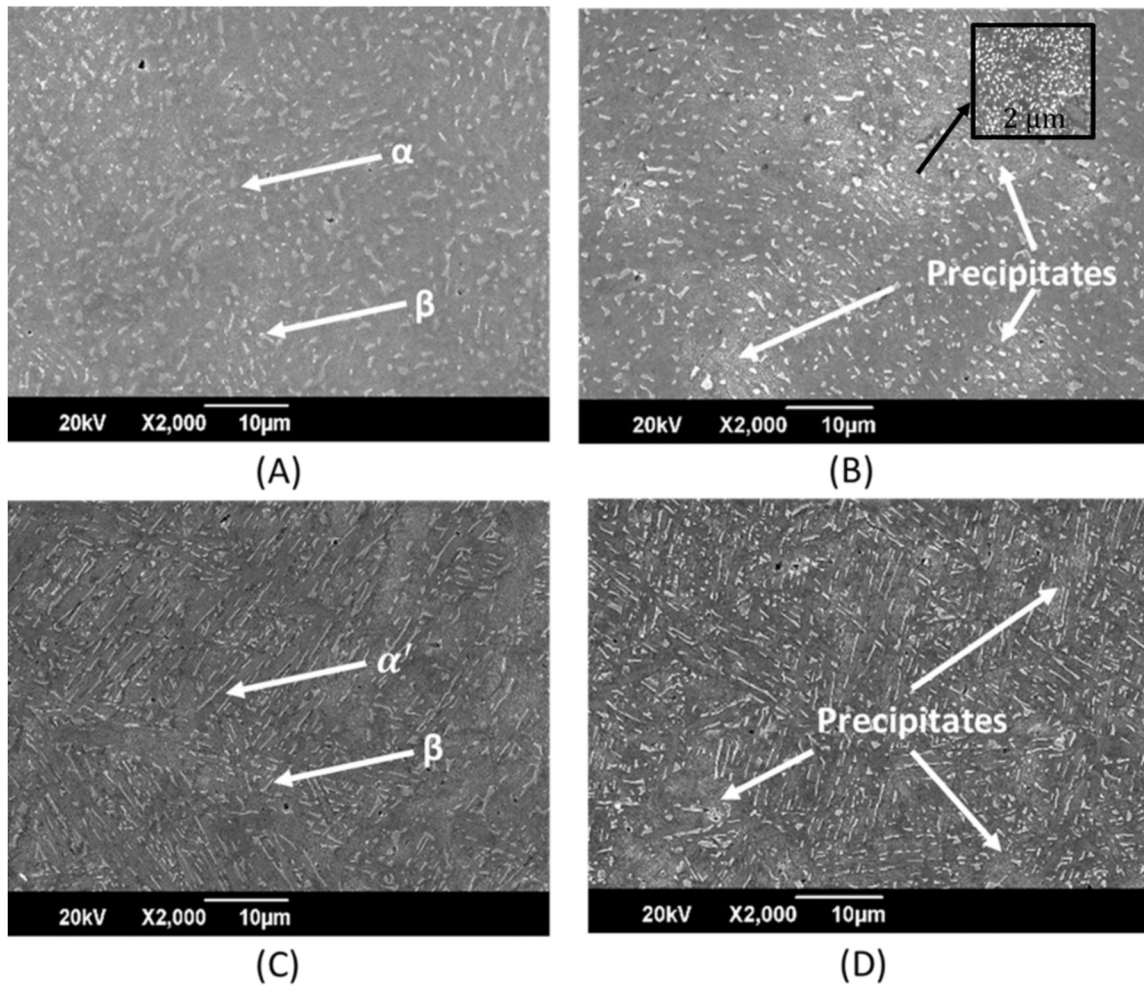
Fig. 3.7. SEM images of Ti-6Al-4V alloy surfaces including (A) CM Ti-6Al-4V, (B) PMF-treated CM Ti-6Al-4V, (C) LPBF-produced Ti-6Al-4V and (D) PMF-treated LPBF-produced Ti-6Al-4V after etching with Kroll's reagent.
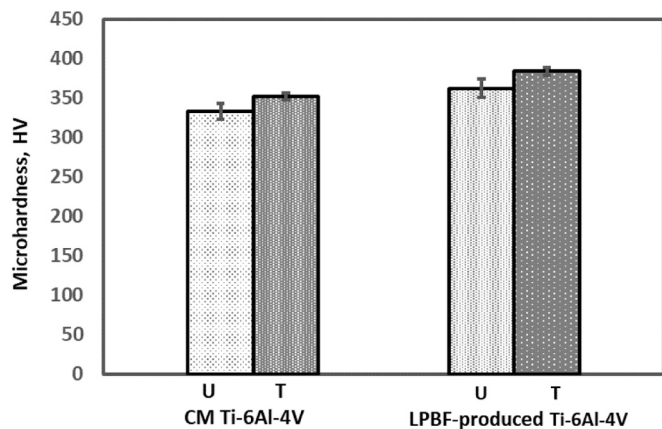

Fig. 3.8. Comparison of microhardness of treated and untreated Ti-6Al-4 V alloys.

As a result of the PMF treatment, the microhardness of the CM and LPBF-produced Ti-6Al4V alloy increased by 5.73% and 5.85%, respectively. The reduction of the mean standard deviation (shown as error bars in Fig. 3.8) of both alloys suggests that there is less scatter in the microhardness results. This observation implies that the microstructure may be becoming more homogeneous. The increase in the microhardness of the Ti-6Al-4V alloy can be linked to the precipitation of fine β which was observed in Fig. 3.7. Such precipitation due to magnetic field treatment was observed in the previous study by Akram et al. [62] in nickel aluminium bronze and aluminium alloy 2014-T6 alloy.

4. Discussion

4.1. Mechanisms driving the improvement in corrosion and cavitation erosion resistance due to pulsed magnetic field treatment

PMF led to improvement in corrosion and cavitation erosion resistance of both the CM and LPBF samples. Previous research studies [5,11, 12,15,16] had demonstrated improvement in the corrosion resistance of 3D-printed Ti-6Al-4V by using heat treatment (HT) which led to the transformation of the α' phase to α and β (with the β phase playing a leading role). This transformation leads to very fine α and β seems to increase the microhardness of the samples. In exploring the effect of PMF treatment, it is important to understand the factors that lead to such phase transformations. One possible cause of phase transformation is the heating of the samples as a result of PMF. The samples experienced a pulsed magnetic field and induced eddy currents. To evaluate the processing parameters, such as magnetic flux density and the subsequent eddy current distribution and their effect on temperature, finite element (FE) numerical simulation was carried out using QuickField 2-D software. Two tasks were simulated: (i) a transient electromagnetic field problem and (ii) the problem of transient heating caused by Joule losses. Tasks were solved in an axisymmetric formulation. Since the real

inductor itself has an axisymmetric design, during the simulation, the geometric details of the model were identical to the real ones; at the same time, the geometry of the sample should be changed to match the axial symmetry. In this case, it was necessary to find the diameter of the equivalent cylindrical sample; the diameter was coaxially located in the centre of the inductor during the simulation. For this, it was necessary to provide equality of the cross-sectional areas, A_r and A_s, of the real and simulated samples that the magnetic field crossed during processing. As the maximum cross-sectional area of the real sample, which was penetrated by the magnetic field flux, was $A_r = d \cdot h = 50\ mm^2$, the cross-section of the simulated sample was set to be the same; $A_s = \pi \cdot r^2 = 50\ mm^2$, therefore, the radius of the sample was taken as $r = 4$ mm. The length of the cylindrical sample in the simulation was set to be 10 mm. It must be noted that simulations with such cylindrical samples do not yield exact distributions of the magnetic flux density, eddy current and temperature and are probably not identical to real-life samples as used during the treatment (tablet-shape oriented as in Fig. 2.1(B)); however, they give an approximation and some understanding of the order of their magnitude during treatment.

The simulations were performed based on the following physical properties of the Ti-6Al-4V alloy [63]: thermal conductivity, $\lambda = 6.7$ W/(m·K); specific heat, $c = 526$ J/(kg·K), density, $\rho = 4430$ kg/m^3 and electrical conductivity, $\sigma = 5.6 \cdot 10^5$ S/m. The material properties were assumed to be independent of temperature during the treatment. The relative permeability was taken to be equal to 1 due to the high magnetic field strength. The initial temperature at the start of the treatment was measured to be 20 °C and heat transfer with ambient air was excluded. A change in the current with time in each turn of the inductor during the modelling was taken in the form of Eq. (1)

$$I(t) = I_0 e^{-at} \sin\left(\frac{2\pi t}{t_{PEC}}\right) \tag{1}$$

where the period t_{PEC} and the value of I_0 were determined from the current recording as presented in Fig. 2.1 (C).

The results of the numerical modelling are presented in Fig. 4.1 which illustrates the variation of the magnetic flux density in the centre of the inductor (sample) and the variation of the induced eddy currents at various locations relative to the axis of the sample ($r_1 = 4$ mm, $r_2 = 2$ mm, $r_3 = 0.001$ mm). The increase of temperature at the outer surface of the sample was thus obtained. It can be concluded that the maximum magnetic flux density at the bore of the inductor was approximately 22 T (Fig. 4.1(A)). The same magnetic field affected the sample by inducing eddy currents. Unlike the magnetic flux density which was more or less uniform inside the inductor bore and the sample, the induced eddy currents were distributed linearly over the cross-section of the sample; a maximum eddy current peak density $j = 6.4 \times 10^8$ A/m^2 was obtained at the surface of the sample along with a minimum peak density of $j = 8 \times 10^7$ A/m^2 near the axis of symmetry (Fig. 4.1(B)). The simulation also predicted that as a result of the application of a single pulse, the outer surface temperature would increase by 28 °C (Fig. 4.1(C)). This modest heating effect was in agreement with thermocouple measurements of the temperature of the samples during PMF treatment. The observed results were, therefore, not caused by the heating of the samples. A non-thermal effect leading to both mobility of atoms and defects like dislocations, as previously reported [64–66] as a result of the application of the magnetic field and the resulting eddy currents, is more likely. Molotskii [64] suggested that the magnetic field plays only a triggering

effect for dislocation motion, but the motion itself takes place due to the latent energy stored in the metal following its manufacture. As a result of his investigation, Molotskii [64] noted that the dislocation-to-paramagnetic obstacles (impurities, vacancies, etc.) bond energy depends on the spin multiplicity of the radical pairs formed by the dislocation core and the obstacles. As the radical pairs may be either in the singlet (with high binding energy) or in the triplet (with low binding energy) spin states, the application of a magnetic field induces
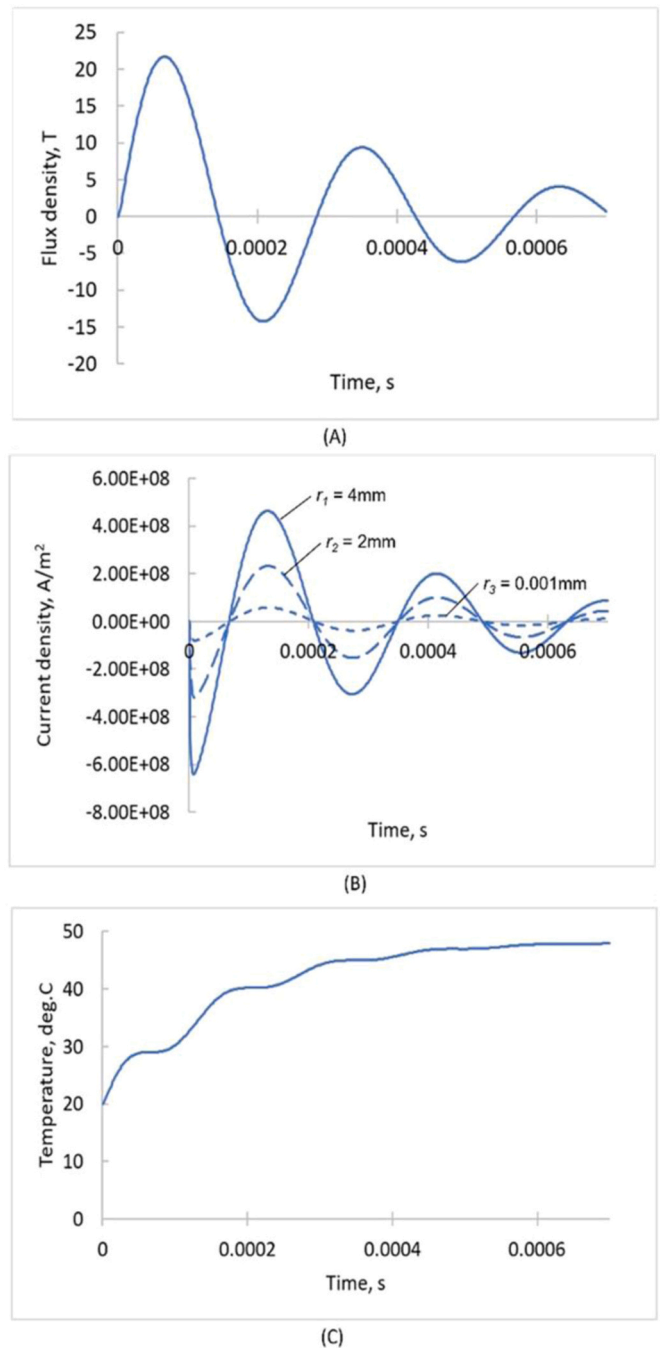
Fig. 4.1. Variation of magnetic field flux density in the centre of inductor (A), induced eddy current density (B) on the outer cylindrical surface and inside the sample, and temperature rise (C) on the outer cylindrical surface of the modelled sample caused by the application of one pulse of magnetic field.

transitions between the singlet and triplet states. Additional populations of the triplet state with weak bonding facilitate the depinning of the dislocations from obstacles and their movement. The mechanism proposed by Molotskii [64] involving the magnetic field inducing transitions from singlet to triplet states could be used to interpret the observations of this study that concerned titanium, which is a paramagnetic metal, and according to the XRD analysis, both the CM and LPBF-produced samples contained some RS (stored energy). Furthermore, the high-density electric current (induced eddy current) itself could promote additional mobility of dislocations as the flowing conductivity electrons can create a backing force for them [64–66] and even

cause their multiplication, as previously demonstrated for pure titanium by Babutskyi et al. [8]. According to Baranov et al. [66], there is a threshold value of electric current density $j > 10^8$ A/m^2 above which electroplastic deformation caused by the current-activated movement of dislocations takes place. The simulation of the treatment showed a maximum eddy current peak density $j = 6.4 \times 10^8$ A/m^2 at the sample surface; this value exceeded the threshold value required to activate the motion of dislocations. It can, therefore, be concluded that during the treatment, conditions for the activation of dislocation movement were created at the surface of the sample. This increased mobility of atoms and particularly of dislocations due to the application of a pulsed magnetic field, induced depinning of dislocations from obstacles in conjunction with a flying electron force. This can explain the observed phase transformation and the changes in the lattice parameters of the samples and the reduction of the tensile RS in the CM alloy. These factors could also cause the increase in the compressive RS in the LPBF alloy because the surface of the sample is a natural sink for dislocations. Such motion causes the accumulation of strains in the surface layer and to the subsequent increase in compressive RS. In the same manner, this treatment can further promote microstructural homogenisation through precipitation as shown in Fig. 3.7 and Fig. 3.8. The observed phase transformation from the metastable α' martensite to the stable α can be considered from the point of view of chemical thermodynamics and the Gibbs Free energy. While this phase transformation can be driven by an increase in the temperature of the system, other variables, like a magnetic field, can also change the state of equilibrium. According to Lewis and Randall [67], the application of a magnetic field can provide an additional contribution to the Gibbs Free energy, ΔG°. This can be presented in the form of Eq. (2),

$$\Delta G^\circ = \Delta G^\circ_{non-magnetic} + \Delta G^\circ_{magnetic\ (internal)} + \Delta G^\circ_{magnetic\ (external)} \tag{2}$$

which shows a magnetic contribution ($\Delta G^\circ_{magnetic\ (external)}$) from an external magnetic field to the value of ΔG°, in addition to an inherent internal magnetic contribution ($\Delta G^\circ_{magnetic\ (internal)}$) and to a non-magnetic contribution ($\Delta G^\circ_{non-magnetic}$). From a chemical thermodynamic point of view, the application of PMF treatment can activate the transformation of the martensitic phase to the two thermodynamically stable phases. Atomic diffusion is needed for the phase transformation to take place and this is related to the PMF current density according to Eq. (3) [68].

$$J = \frac{2NeZ^*D\rho J_m f \tau_p}{\pi kT} \tag{3}$$

where J is the atomic flux, N is the atom concentration of a given element, e is the charge of an electron, Z^* is the effective valence of the metals, D is the diffusion coefficient, ρ is the electrical resistivity of the alloy, J_m is the current density of the PMF treatment, f is the frequency of the PMF treatment, τ_p is the duration of the PMF treatment, k is the Boltzmann constant and T is the temperature. Therefore, the atomic flux is directly proportional to the current density generated by the PMF treatment. Thus, the use of PMF treatment can induce atomic diffusion and activate the transformation of α' martensite to the α and β phases. These results unambiguously show that the transition from a less noble state to a more noble one takes place. This is also reflected when RS are considered (see for example Table 3.4) and there is a correlation with the level and sign of RS at the sample surface. Surface RS have a paramount importance on the corrosion of metals both at the macro- and microlevels as the presence of tensile RS shift the surface potential to a more electronegative state thus increasing the tendency to corrode [6, 69–71]. For example, Van Boven et al. [70] showed that corrosion occurs in areas of high tensile RS, in contrast to areas with compressive RS, where corrosion is practically absent. The beneficial effect of compressive RS on the formation and maintenance of the passive oxide film has been reported for stainless steels [7,72] and aluminium alloys [73]. The presence of compressive RS creates a more compact alloy surface with

fewer defects like pores, pits and cracks and indeed compressive RS can close and heal such defects. The effect of this is to minimise the access of the corroding medium (oxygen and water) into the alloy; for corrosion to progress, it is necessary for oxygen to migrate into the alloy and the absence of pits and pores is going to limit the rate of this movement. For the same reason, a more compact alloy surface due to the presence of compressive RS can be expected to have more resistance to electronic charge transfer which will lead to a reduction in the rate of corrosion. Following the PMF treatment, the final distribution of RS within the surface regions of the treated samples of both the conventionally-produced and LPBF-manufactured Ti-6Al-4V, facilitated the development of a more adherent (due to the absence or reduction of defects) and stable passive film on the alloy surface, and this provided improved corrosion resistance. A similar correlation exists between the level of erosion of metals and RS at their surface; the transition from a more eroded metal to a less eroded one (see data for mass loss in Table 3.3) is in exact correlation with the nature of the RS at the alloy surface (Table 3.4). As in the above case, the beneficial effect of compressive RS on inhibiting cavitation erosion is widely reported [58, 74]. Thus, the PMF treatment has the potential to improve the performance of the Ti-6Al-4V alloy under corrosion and erosion operating conditions.

Taking these observations and conclusions into account, PMF treatment seems to be a quick, low-energy and cost-effective technique that can lead to improvement in the behaviour of 3D-printed Ti-6Al-4V. Potentially, PMF can, in the future, replace heat treatment as a processing technique. It is clear that further research is required to fully understand the effect of PMF treatment on the microstructure of the treated alloys in order to develop the technique into a commercial process. Further examination of the effect of PMF treatment on the defect structure by using microscopic techniques is required. Additional electrochemical investigation is also needed to further unlock the understanding of how PMF post-processing affects corrosion behaviour. Such investigations will be the focus of future studies by the authors.

5. Conclusions

The application of pulsed magnetic field (PMF) treatment demonstrated enhanced resistance to corrosion and cavitation erosion in Ti-6Al-4V alloys produced through both conventional manufacturing (CM) and laser-based powder bed fusion (LPBF) methods. Based on the results of the present study, the following conclusions can be drawn:

1. The application of PMF treatment led to enhanced corrosion resistance in both conventionally manufactured (CM) and laser powder bed fusion (LPBF)-produced Ti-6Al-4V. The observed effect can be attributed to:

   (i) the formation of a more stable and denser passive film following the treatment with PMF,

   (ii) a reduction in the amount of the metastable acicular martensite (α') phase by 0.13%, which is observed through the transformation into the stable α and β phases in LPBF-produced Ti-6Al-4V,

   (iii) an increase in dislocations on the surface of the alloy samples which led to an elevation in compressive residual stress (RS) in LPBF-produced Ti-6Al-4V.

   (iv) a decrease in tensile RS in the case of CM Ti-6Al-4V, and

   (v) a reduction in the standard deviation of the microhardness results indicating the formation of a more homogeneous microstructure.

2. The use of PMF treatment resulted in a decrease in the occurrence of surface cavitation erosion in LPBF and CM Ti-6Al-4V materials by 15.04% and 17.99% respectively, as compared to samples that were not subjected to any treatment. The observed decrease in cavitation erosion can be attributed to a corresponding increase in

microhardness by 5.85% for LPBF Ti-6Al-4V and 5.73% for CM Ti-6Al-4V due to an increase in the density of dislocations at the surface of the alloys.

3. The application of the PMF treatment resulted in the activation of dislocation motions and enabled their depinning from obstacles. The observed phenomenon can be ascribed to an increased population of triplet spin states, characterised by weak bonding, within radical pairs that are produced by the barriers and the dislocation core. The presence of induced eddy currents, particularly on the external surface of the sample, exerted an extra force on the dislocations, thereby facilitating their movement. The aforementioned observations are responsible for alterations in the lattice parameters of the alloys, resulting in a reduction in the tensile residual stress and an increase in the compressive residual stress at the surfaces of the samples.

Author statement

I, Dr Ma Mohin (Corresponding Author), declare that this manuscript is original, has not been published before and is not currently being considered for publication elsewhere.

I confirm that the manuscript has been read and approved by all named authors and that there are no other persons who satisfied the criteria for authorship but are not listed. I further confirm that the order of authors listed in the manuscript has been approved by all of us.

I understand that the Corresponding Author is the sole contact for the Editorial process. I am responsible for communicating with the other authors about progress, submissions of revisions and final approval of proofs.

CRediT authorship contribution statement

Andreas Chrysanthou: Writing – review & editing, Writing – original draft, Visualization, Validation, Supervision, Software, Resources, Project administration, Methodology, Investigation, Funding acquisition, Formal analysis, Conceptualization. **Sufyan Akram:** Writing – review & editing, Writing – original draft, Visualization, Validation, Software, Resources, Methodology, Investigation, Funding acquisition, Formal analysis, Data curation, Conceptualization. **Aidan M. Doyle:** Writing – review & editing, Writing – original draft, Visualization, Validation, Supervision, Software, Resources, Project administration, Methodology, Investigation, Funding acquisition. **Ma Mohin:** Writing – review & editing, Writing – original draft, Visualization, Validation, Supervision, Software, Resources, Project administration, Methodology, Investigation, Funding acquisition, Formal analysis, Data curation, Conceptualization. **Edward P. Randviir:** Writing – review & editing, Writing – original draft, Visualization, Validation, Software, Resources, Methodology, Investigation, Formal analysis. **Anatolii Babutskyi:** Writing – review & editing, Writing – original draft, Visualization, Validation, Software, Resources, Methodology, Investigation, Funding acquisition, Formal analysis, Conceptualization.

Declaration of Competing Interest

The authors declare that they have no known competing financial interests or personal relationships that could have appeared to influence the work reported in this paper.

Data availability

The authors are unable or have chosen not to specify which data has been used.

Acknowledgements

Dedication

This paper is dedicated to the memory of Dr Anatolii Babutskyi.

References

[1] E.E. Billinghurst Jr, Tensile Properties of Cast Titanium Alloys: Titanium-6Al-4V ELI and Titanium-5Al-2.5 Sn ELI, 1992.

[2] C.N. Elias, J. Lima, R. Valiev, M.A. Meyers, Biomedical applications of titanium and its alloys, JOM 60 (2008) 46–49.

[3] N. Dai, L. Zhang, J. Zhang, Q. Chen, M. Wu, Corrosion behavior of selective laser melted Ti-6Al-4 V alloy in NaCl solution, Corros. Sci. 102 (2016) 484–489.

[4] Y. Bai, X. Gai, S. Li, L. Zhang, Y. Liu, Y. Hao, X. Zhang, R. Yang, Y. Gao, Improved corrosion behaviour of electron beam melted Ti-6Al–4V alloy in phosphate buffered saline, Corros. Sci. 123 (2017) 289–296.

[5] A.H. Ettefagh, C. Zeng, S. Guo, J. Raush, Corrosion behavior of additively manufactured Ti-6Al-4V parts and the effect of post annealing, Addit. Manuf. 28 (2019) 252–258.

[6] J.J. Harwood, The influence of stress on corrosion (part 1 of two parts), Corrosion 6 (1950) 249–259.

[7] O. Takakuwa, H. Soyama, Effect of residual stress on the corrosion behavior of austenitic stainless steel, Adv. Chem. Eng. Sci. 5 (2014) 62.

[8] A. Babutskyi, A. Chrysanthou, M. Smelina, G. Stepanov, M. Ziętara, Effect of pulsed magnetic treatment on the corrosion of titanium, Mater. Sci. Technol. 33 (2017) 1461–1472.

[9] N. Dai, L. Zhang, J. Zhang, X. Zhang, Q. Ni, Y. Chen, M. Wu, C. Yang, Distinction in corrosion resistance of selective laser melted Ti-6Al-4V alloy on different planes, Corros. Sci. 111 (2016) 703–710.

[10] N. Dai, J. Zhang, Y. Chen, L. Zhang, Heat treatment degrading the corrosion resistance of selective laser melted Ti-6Al-4V alloy, J. Electrochem. Soc. 164 (2017) C428.

[11] P. Chandramohan, S. Bhero, B.A. Obadele, P.A. Olubambi, Laser additive manufactured Ti–6Al–4V alloy: tribology and corrosion studies, Int. J. Adv. Manuf. Technol. 92 (2017) 3051–3061.

[12] P. Chandramohan, S. Bhero, K. Manikandasubramanian, B. Ravishankar, A review of additive manufacturing of α-β Ti alloy components through selective laser melting and laser metal deposition, J. Eng. Sci. Technol. 13 (2018) 790–812.

[13] L.Y. Chen, J.C. Huang, C.H. Lin, C.T. Pan, S.Y. Chen, T.L. Yang, D.Y. Lin, H.K. Lin, J. Jang, Anisotropic response of Ti-6Al-4V alloy fabricated by 3D printing selective laser melting, Mater. Sci. Eng. A 682 (2017) 389–395.

[14] J.J. De Damborenea, M.A. Arenas, M.A. Larosa, A.L. Jardini, C.A. de Carvalho Zavaglia, A. Conde, Corrosion of Ti6Al4V pins produced by direct metal laser sintering, Appl. Surf. Sci. 393 (2017) 340–347.

[15] Y. Xu, Y. Lu, K.L. Sundberg, J. Liang, R.D. Sisson, Effect of annealing treatments on the microstructure, mechanical properties and corrosion behavior of direct metal laser sintered Ti-6Al-4V, J. Mater. Eng. Perform. 26 (2017) 2572–2582.

[16] J. Yang, H. Yang, H. Yu, Z. Wang, X. Zeng, Corrosion behavior of additive manufactured Ti-6Al-4V alloy in NaCl solution, Metall. Mater. Trans. A 48 (2017) 3583–3593.

[17] Q. Sui, P. Li, K. Wang, X. Yin, L. Liu, Y. Zhang, Q. Zhang, S. Wang, L. Wang, Effect of build orientation on the corrosion behavior and mechanical properties of selective laser melted Ti-6Al-4V, Metals 9 (2019) 976.

[18] J. Fojt, M. Fousova, E. Jablonska, L. Joska, V. Hybasek, E. Pruchova, D. Vojtech, T. Ruml, Corrosion behaviour and cell interaction of Ti-6Al-4V alloy prepared by two techniques of 3D printing, Mater. Sci. Eng. C 93 (2018) 911–920.

[19] D. Kong, C. Dong, X. Ni, X. Li, Corrosion of metallic materials fabricated by selective laser melting, npj Mater. Degrad. 3 (2019) 24.

[20] G. Sander, J. Tan, P. Balan, O. Gharbi, D.R. Feenstra, L. Singer, S. Thomas, R. G. Kelly, J.R. Scully, N. Birbilis, Corrosion of additively manufactured alloys: a review, Corrosion 74 (2018) 1318–1350.

[21] X. Gong, Y. Cui, D. Wei, B. Liu, R. Liu, Y. Nie, Y. Li, Building direction dependence of corrosion resistance property of Ti–6Al–4V alloy fabricated by electron beam melting, Corros. Sci. 127 (2017) 101–109.

[22] H. Li, Z. Cui, Z. Li, S. Zhu, X. Yang, Effect of gas nitriding treatment on cavitation erosion behavior of commercially pure Ti and Ti– 6Al– 4V alloy, Surf. Coat. Technol. 221 (2013) 29–36.

[23] I. Mitelea, E. Dimian, I. Bordeaşu, C. Crăciunescu, Ultrasonic cavitation erosion of gas nitrided Ti–6Al–4V alloys, Ultrason. Sonochem. 21 (2014) 1544–1548.

[24] J. Kaspar, J. Bretschneider, S. Jacob, S. Bonß, B. Winderlich, B. Brenner, Microstructure, hardness and cavitation erosion behaviour of Ti–6Al–4V laser nitrided under different gas atmospheres, Surf. Eng. 23 (2007) 99–106.

[25] J.M. Robinson, S. Anderson, R.D. Knutsen, R.C. Reed, Cavitation erosion of laser l11eltedand laser nitrided Ti–6Al–4V, Mater. Sci. Technol. 11 (1995) 611–618.

[26] M. Khorasanian, M. Yeganeh, S.R.A. Zaree, Microstructure and corrosion performance of plasma electrolytic oxidation coatings on the surface of conventional and selective laser melted Ti-6Al-4V alloy, Surf. Topogr. Metrol. Prop. 10 (2022) 035046.

[27] P.B. Santos, V.V. de Castro, E.K. Baldin, C. Aguzzoli, G.A. Longhitano, A.L. Jardini, É.S.N. Lopes, A.M.H. de Andrade, C. de Fraga Malfatti, Wear resistance of plasma electrolytic oxidation coatings on Ti-6Al-4V Eli alloy processed by additive manufacturing, Metals 12 (2022) 1070.

[28] H. Sasaki, F. Takeo, H. Soyama, Cavitation erosion resistance of the titanium alloy Ti–6Al–4V manufactured through additive manufacturing with various peening methods, Wear 462 (2020) 203518.

[29] A. Ručinskien, G. Bikulčius, L. Gudavičiūt, E. Juzeliūnas, Magnetic field effect on stainless steel corrosion in FeCl3 solution, Electrochem. Commun. 4 (2002) 86–91.

[30] H. Liu, T. Gu, G. Zhang, Y. Cheng, H. Wang, H. Liu, The effect of magneticfield on biomineralization and corrosion behavior of carbon steel induced by iron-oxidizing bacteria, Corros. Sci. 102 (2016) 93–102.

[31] R. Burrows, A. Baron-Wiechec, C. Harrington, S. Moore, D. Chaney, T.L. Martin, J. Likonen, R. Springell, E. Surrey, The possible effect of high magnetic fields on the aqueous corrosion behaviour of Eurofer, Fusion Eng. Des. 136 (2018) 1000–1006.

[32] X. Huang, Residual stress reduction by combined treatment of pulsed magnetic field and pulsed current, Mater. Sci. Eng. A 528 (2011) 6287–6292.

[33] Q. Shao, J. Kang, Z. Xing, H. Wang, Y. Huang, G. Ma, H. Liu, Effect of pulsed magnetic field treatment on the residual stress of 20Cr2Ni4A steel, J. Magn. Magn. Mater. 476 (2019) 218–224.

[34] A.L. Lu, F. Tang, X.J. Luo, J.F. Mei, H.Z. Fang, Research on residual-stress reduction by strong pulsed magnetic treatment, J. Mater. Process. Technol. 74 (1998) 259–262.

[35] X. Xi, Y. Xia, Y. Hu, The effects of magnetic treatment on the tribological behavior of AISI 1045 steel under lubricated conditions, Tribol. Trans. 61 (2018) 671–682.

[36] A. Babutskyi, A. Chrysanthou, C. Zhao, Effect of pulsed magnetic field pre-treatment of AISI 52100 steel on the coefficient of sliding friction and wear in pin-on-disk tests, Friction 2 (2014) 310–316.

[37] A. Standard, G32-10, Standard Test Method for Cavitation Erosion Using Vibratory Apparatus, Annual Book of ASTM Standards; ASTM: West Conshohocken, PA, USA, 2010, pp. 1–10.

[38] Materialise, Titanium (Ti6Al4V), 2019.

[39] A. Standard, B74.18: Grading Of Certain Abrasive Grain On Coated Abrasive Products, 1996.

[40] D. Cseh, V. Mertinger, X-Ray Diffraction Measurements of Residual Stress Induced by Surface Compressing Methods, 729, 2013, pp. 199–204.

[41] L. Zeng, T.R. Bieler, Effects of Working, Heat Treatment, and Aging on Microstructural Evolution and Crystallographic Texture of α, α′, α″ and β Phases in Ti–6Al–4V Wire, 392, 2005, pp. 403–414.

[42] V.A. Alves, R.Q. Reis, I. Santos, D.G. Souza, Td.F. Gonçalves, M.A. Pereira-da-Silva, A. Rossi, L.A. Da Silva, In situ impedance spectroscopy study of the electrochemical corrosion of Ti and Ti–6Al–4V in simulated body fluid at 25C and 37C, Corros. Sci. 51 (2009) 2473–2482.

[43] S.B. Arya, F.J. Joseph, Electrochemical methods in tribocorrosion. Tribocorrosion, Elsevier, 2021, pp. 43–77.

[44] E. McCafferty, Validation of corrosion rates measured by the Tafel extrapolation method, Corros. Sci. 47 (2005) 3202–3215.

[45] F.X. Xie, X.B. He, S.L. Cao, X. Lu, X.H. Qu, Structural characterization and electrochemical behavior of a laser-sintered porous Ti–10Mo alloy, Corros. Sci. 67 (2013) 217–224.

[46] M.P. Pujadó. Carbon Nanotubes as Platforms for Biosensors with Electrochemical and Electronic Transduction, Springer Science & Business Media, 2012.

[47] M. Prestat, D. Thierry, 2021, Corrosion of Titanium under Simulated Inflammation Conditions: Clinical Context and in Vitro Investigations, 136, 2021, pp. 72–87.

[48] Q. Luo, Q. Zhang, Z. Qin, Z. Wu, B. Shen, L. Liu, W. Hu, The synergistic effect of cavitation erosion and corrosion of nickel-aluminum copper surface layer on nickel-aluminum bronze alloy, J. Alloy. Compd. 747 (2018) 861–868.

[49] I. Park, S. Kim, Effect of pH of the sulfuric acid bath on cavitation erosion behavior in natural seawater of electroless nickel plating coating, Appl. Surf. Sci. 483 (2019) 194–204.

[50] G. Taillon, F. Pougoum, S. Lavigne, L. Ton-That, R. Schulz, E. Bousser, S. Savoie, L. Martinu, J. Klemberg-Sapieha, Cavitation Erosion Mechanisms in Stainless Steels and in Composite Metal–ceramic HVOF Coatings, 364, 2016, pp. 201–210.

[51] C. Zhang, C. Wu, S. Zhang, Y. Jia, M. Guan, J. Tan, B. Lin, Laser Cladding of NiCrSiB on Monel 400 to Enhance Cavitation Erosion and Corrosion Resistance, 41, 2022, pp. 4257–4265.

[52] M.K. Zadeh, M. Yeganeh, M.T. Shoushtari, H. Ramezanalizadeh, F. Seidi, Microstructure, Corrosion Behavior, and Biocompatibility of Ti-6Al-4 V Alloy Fabricated by LPBF and EBM Techniques, 31, 2022, 103502.

[53] M. Yeganeh, M.T. Shoushtari, A.T. Khanjar, N.H.J. Al Hasan, , Microstructure evolution, corrosion behavior, and biocompatibility of Ti-6Al-4V alloy manufactured by electron beam melting (EBM) technique, Colloids Surf. Physicochem. Eng. Asp. 679 (2023) 132519.

[54] S. Sinha, S.S. Nene, M. Frank, K. Liu, P. Agrawal, R.S. Mishra, On the Evolving Nature of c/a Ratio in A Hexagonal Close-packed Epsilon Martensite Phase in Transformative High Entropy Alloys, 9, 2019, 13185.

[55] D. Hart, D. Whale, A Review of Cavitation-erosion Resistant Weld Surfacing Alloys for Hydroturbines, 8, 2007, pp. 180–187.

[56] L. Bai, K. Jiang, L. Gao, The Influence and Mechanism of Residual Stress on the Corrosion Behavior of Welded Structures, 21, 2018.

[57] Z. Pędzich, R. Jasionowski, M. Ziąbka, Cavitation Wear of Structural Oxide Ceramics and Selected Composite Materials, 34, 2014, pp. 3351–3356.

[58] Z. Tong, J. Jiao, W. Zhou, Y. Yang, L. Chen, H. Liu, Y. Sun, X. Ren, 2019, Improvement in Cavitation Erosion Resistance of AA5083 Aluminium Alloy by Laser Shock Processing, 377, 2019, 124799.

[59] S. Hanke, M. Beyer, A. Silvonen, J.F. Dos Santos, A. Fischer, 2013, Cavitation Erosion of Cr60Ni40 Coatings Generated by Friction Surfacing, 301, 2013, pp. 415–423.

[60] B. Vrancken, L. Thijs, J. Kruth, J. Van Humbeeck, Heat treatment of Ti6Al4V produced by selective laser melting: microstructure and mechanical properties, J. Alloy. Compd. 541 (2012) 177–185.

[61] E. Sallica-Leva, R. Caram, A.L. Jardini, J.B. Fogagnolo, Ductility Improvement Due to Martensite α′ Decomposition in Porous Ti–6Al–4V Parts Produced by Selective Laser Melting for Orthopedic Implants, 54, 2016, pp. 149–158.

[62] S. Akram, A. Babutskyi, A. Chrysanthou, D. Montalvão, M.J. Whiting, N. Pizurova, 2021, Improvement of the Wear Resistance of Nickel-aluminium Bronze and 2014-T6 Aluminium Alloy by Application of Alternating Magnetic Field Treatment, 480, 2021, 203940.

[63] MatWeb, Titanium Ti-6Al-4V (Grade 5), Annealed, 2019.

[64] M.I. Molotskii, Theoretical Basis for Electro-and Magnetoplasticity, 287, 2000, pp. 248–258.

[65] H. Conrad, Electroplasticity in Metals and Ceramics, 287, 2000, pp. 276–287.

[66] Y.V. Baranov, O.A. Troitskii, Y.S. Avraamov, A.D. Shlyapin, Physical Bases of Electric-pulse and Electroplastic Treatments and New Materials, 1, 2001, pp. 56–77.

[67] G.N. Lewis, Randall, Thermodynamics and the Free Energy of Chemical Substances, 1923.

[68] Y. Jiang, G. Tang, L. Guan, S. Wang, Z. Xu, C. Shek, Y. Zhu, Effect of electropulsing treatment on solid solution behavior of an aged Mg alloy AZ61 strip, J. Mater. Res. 23 (2008) 2685–2691.

[69] N.P. Zhuk, A Course of Corrosion and Protection of Metals, 1968 (in Russian).

[70] G. Van Boven, W. Chen, R. Rogge, The role of residual stress in neutral pH stress corrosion cracking of pipeline steels. Part I: pitting and cracking occurrence, Acta Mater. 55 (2007) 29–42.

[71] R. Oltra, V. Vignal, Recent advances in local probe techniques in corrosion research–analysis of the role of stress on pitting sensitivity, Corros. Sci. 49 (2007) 158–165.

[72] P. Peyre, X. Scherpereel, L. Berthe, C. Carboni, R. Fabbro, G. Béranger, C. Lemaitre, Surface modifications induced in 316L steel by laser peening and shot-peening. Influence on pitting corrosion resistance, Mater. Sci. Eng. A 280 (2000) 294–302.

[73] X. Liu, G.S. Frankel, Effects of compressive stress on localized corrosion in AA2024-T3, Corros. Sci. 48 (2006) 3309–3329.

[74] L. Zhang, Y.K. Zhang, J.Z. Lu, F.Z. Dai, A.X. Feng, K.Y. Luo, J.S. Zhong, Q.W. Wang, M. Luo, H. Qi, Effects of laser shock processing on electrochemical corrosion resistance of ANSI 304 stainless steel weldments after cavitation erosion, Corros. Sci. 66 (2013) 5–13.